



Block-based multispectral image registration with application to spectral color measurement

Hui-Liang Shen^a, Zhe Zou^a, Yufang Zhu^b, Shijian Li^{c,*}

^a College of Information Science and Electronic Engineering, Zhejiang University, Hangzhou 310027, China

^b College of Computer Science and Information Engineering, Zhejiang Gongshang University, Hangzhou 310018, China

^c College of Computer Science, Zhejiang University, Hangzhou 310027, China

ARTICLE INFO

Keywords:

Multispectral imaging
Inter-band misalignment
Image registration
Color measurement

ABSTRACT

A filter-wheel multispectral imaging system can be used to acquire the spectral reflectance of a sample. In the imaging system, large displacements between band images are obtained and corrected by employing a specific chart as a system calibration process. However, small misalignment can still occur due to the possible mechanical vibration when measuring individual samples. These small misalignments always cause chromatic aberration and corrupt spectral accuracy in the acquired multispectral image. To deal with this problem, this paper proposes a block-based multispectral image registration method that is accurate and efficient for practical color measurement. In our method, each band image is evenly divided into blocks. The local translations between individual block pairs, which are selected according to a gradient strength map, are computed based on an image similarity measure. The misalignment between reference and floating band images is modeled as a global affine transform, which can be efficiently solved using regularized least squares. Experimental results validate the accuracy and computational efficiency of our method on both synthetic and real images. It is also demonstrated that the accuracy of single-yarn spectral color measurement can be considerably improved by employing our multispectral image registration method.

1. Introduction

Multispectral color imaging has been widely used in color measurement [1], remote sensing [2], and biomedicine [3] fields. Compared with conventional RGB cameras, a multispectral imaging system acquires band images at multiple wavelengths so that more spectral information can be obtained. Based on faithful spectrum reconstruction, accurate color reproduction as well as high-fidelity color images can be guaranteed, which is essential for spectral color measurement [4].

A multispectral imaging system splits the visible spectrum reflected from the imaged object into more than three bands, and records these bands as a series of monochrome images. Various filters can be used to split the spectrum, such as bandpass optical filters [5], the liquid crystal tunable filter (LCTF) [6], and the acousto-optic tunable filter (AOTF) [7]. The imaging system acquires spectral band images sequentially by exchanging filters. Recently, snapshot multispectral imaging systems [8–10] have been developed to capture images at different wavelengths simultaneously.

In this work, we use a filter-wheel multispectral imaging system as shown in Fig. 1. The system consists of a monochrome camera, a lens with 50 mm fixed focal length, and a filter wheel installed with 16 narrowband filters. The full width at half maximum (FWHM) value of

each filter is 10 nm, and the central wavelengths are at 400, 420, ..., and 700 nm. A multispectral image is acquired by rotating the bandpass filters into the optical path and capturing band images sequentially. The spectral reflectance for each pixel in the multispectral image can be reconstructed using Wiener estimation [4].

The filter-wheel imaging system acquires band images with high quality. However, as the effective focal lengths vary at different bands, out-of-focus blur will appear in band images. In addition, due to the non-coplanar placement and different refractive indices of the filters, band images can be misaligned. These two problems preclude the direct combination of band images for further applications. We note that the out-of-focus blur problem can be resolved by computing the optimal focus position for each band and moving the lens using a step motor [11]. Recently, an out-of-focus deblurring algorithm [12] has also been introduced for multispectral images. Hence in this work we focus on the problem of inter-band image misalignment.

In the literature, optical design and post-processing approaches have been introduced to compensate chromatic aberration. An overview of color correction strategies in optical design is presented in [13]. Chromatic aberration in optical systems with five spectral bands is reduced by using a glass selection method [14]. The aberration in

* Corresponding author.

E-mail addresses: shenhl@zju.edu.cn (H.-L. Shen), shijianli@zju.edu.cn (S. Li).

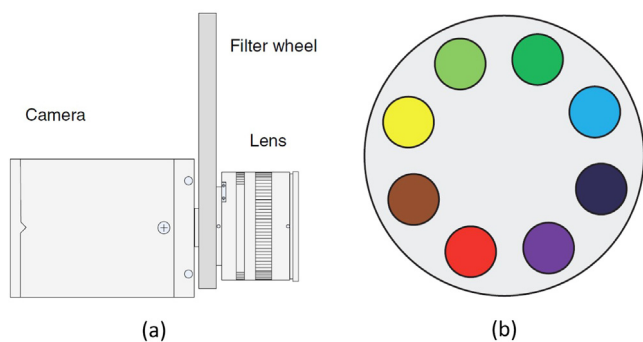


Fig. 1. The schematic diagrams of the multispectral imaging system (a) and the filter wheel (b). Note that the filter wheel employed in this work actually has 16 filters but only 8 ones are drawing for illustration purpose.

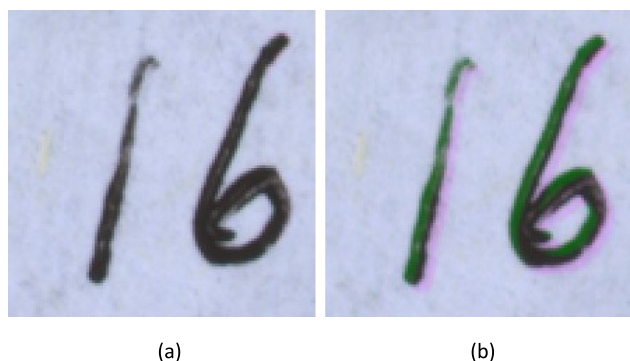


Fig. 2. Chromatic aberration caused by band image misalignment. (a) Original well-aligned multispectral image, (b) Multispectral image by imposing a 3-pixel translation at band 500 nm. The multispectral images are displayed in RGB for illustration purpose.

AOTF can also be corrected with a designed prism [15] or transducers [16]. Post-processing approaches usually aim to find the transform between different bands. A mathematical model of the distortions of band images is derived in [17] and the transform parameters are estimated through image registration. By adopting a particular calibration chart, geometric calibration can be conducted to compensate misalignment [18,19].

In our filter-wheel multispectral imaging system, we correct geometric distortion caused by lens and filters in the systematic calibration procedure. However, we notice that small inter-band misalignment still occurs when measuring samples. This is due to the unavoidable mechanical disturbance during the measurement process, including filter-wheel rotation, lens auto-focus adjustment, slight sample movement, and vibration of surrounding environment. As the induced misalignment is time-variant and not systematic, band image registration should be conducted at the time of acquiring images for individual samples. Actually, this problem also occurs in other sequential imaging systems. For example, the AOTF-based multispectral imaging system suffers from the inter-band misalignment induced by platform jitter [20]. The registration of multispectral images is needed for endoscopes due to the movement of the tissue and camera during acquisition [21].

For high-fidelity appearance reproduction and accurate spectral color measurement, the elimination of the induced misalignment is an urgent need. We illustrate this by a simulation. The original multispectral image (displayed in RGB format) in Fig. 2(a) is well aligned. By inducing a 3-pixel translation, the resultant image in Fig. 2(b) exhibits obvious chromatic aberration.

In this paper, we propose a block-based multispectral image registration method to eliminate the inter-band misalignment. First, each band image is evenly divided into blocks. The blocks with relatively large gradient strength values are selected, and the local translations

between block pairs are computed using an image similarity measure. Then, a global affine transform model is adopted to efficiently estimate the misalignment between reference and floating band images. In the experiments, the proposed registration method is evaluated on both synthetic and real images, and its application to spectral color measurement is demonstrated.

2. Prior art

Image registration aims to find the transform between two images and to make them aligned with each other. Image registration can be categorized into feature-based and intensity-based methods. Feature-based methods usually include the feature detection, extraction, matching, and image transform steps. Among these methods, the most popular is scale invariant feature transform (SIFT) [22]. Feature-based methods are relatively efficient but have limited accuracy, and may fail in multispectral image registration due to luminance change and contrast reversal.

In intensity-based methods, an intensity similarity measure is first defined, and then the correspondence is computed by maximizing a similarity measure between two images. The common similarity measures include sum-of-squared differences (SSD), correlation coefficient (CC), mutual information (MI) and their variations. However, these measures are sensitive to local intensity variation which is common in multispectral images. In [23], the robust selective normalized cross correlation (RSNCC) is proposed for the dense matching of both multispectral and natural images. Recently, the normalized total gradient (NTG) [24], which is based on the sparse characteristics of image gradients, has been introduced for robust multispectral image registration.

After choosing the similarity measure, image registration is cast as an optimization problem of finding optimal transform. As the objective function may be non-convex, the local optimization algorithms such as gradient descent and Levenberg–Marquardt (LM) algorithm [25] may fail to find the optimal transform. The global optimization algorithms such as simulated annealing [26] and evolutionary algorithm [27], on the other hand, suffer from slow convergence rates. As global optimization algorithms are computationally expensive, they are usually unqualified for time critical applications.

Block matching, as an alternative strategy, has been employed in many image registration procedures [17,28,29]. Inspired by this strategy, here we propose a block-based registration method to eliminate small misalignments between spectral band images effectively and efficiently. Our method computes image similarity on selected small-size block pairs instead of the whole image and can produce subpixel accuracy. Based on the estimated translations between block pairs, multispectral image registration is solved in a closed form. Compared with the traditional local and global optimization methods applied on whole images, our method is computationally efficient and avoids the risk of falling into local minimum.

3. Proposed multispectral image registration method

In a multispectral imaging system, the misalignments between band images can be compensated using image registration. Unlike unimodal images, in our application scenario, the image intensities at individual spectral bands can be much different. Besides, the local contrast of two band images may be inconsistent or even reversed [24]. To address these issues, we develop our block-based multispectral image registration method.

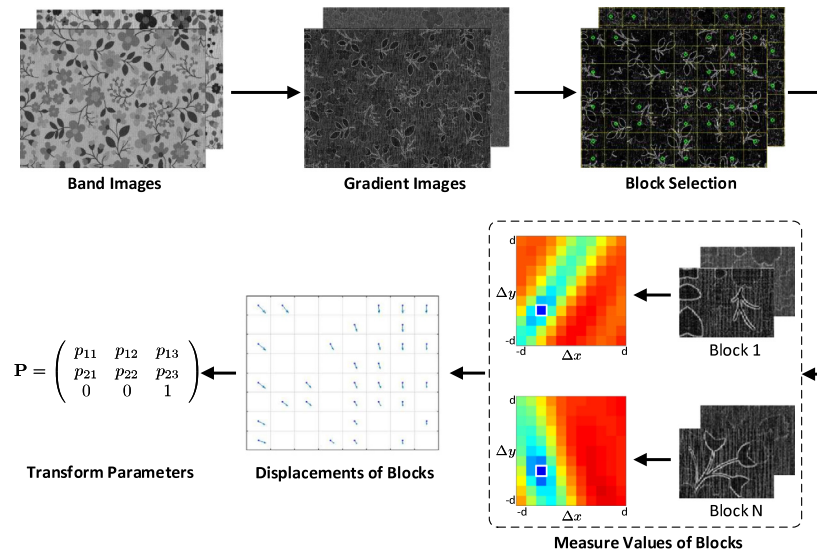


Fig. 3. Framework of our multispectral image registration method . (For interpretation of the references to color in this figure legend, the reader is referred to the web version of this article.)

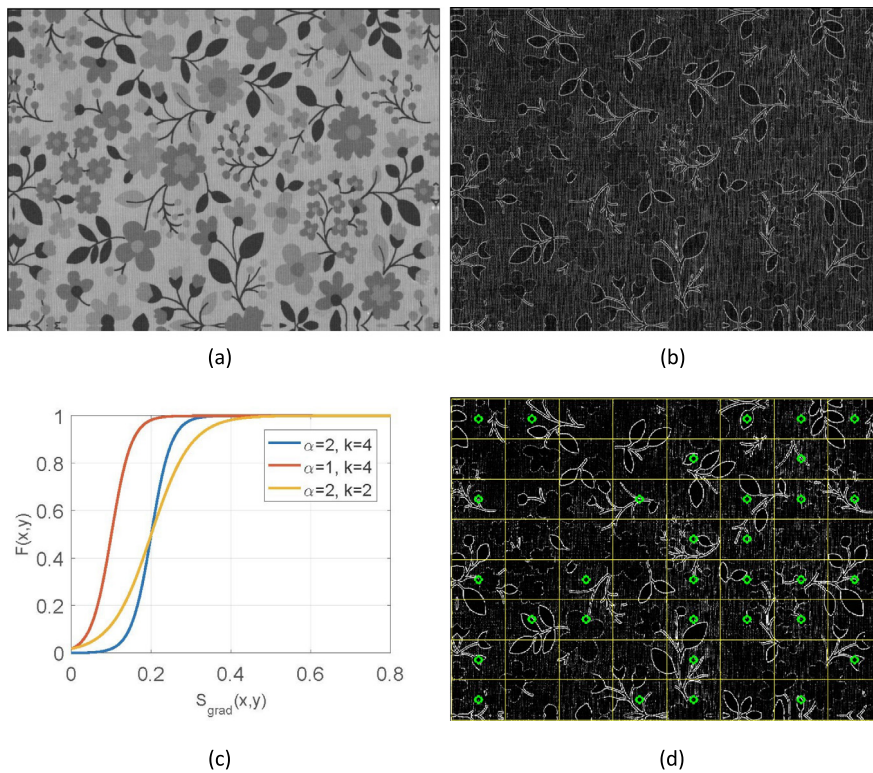


Fig. 4. Image division and block selection of a band image. (a) Original band image, (b) gradient image, (c) The function of $F(x, y)$ w.r.t. $S_{grad}(x, y)$ with different α and k values, (d) gradient strength map F when setting $\alpha = 2$ and $k = 4$. The selected blocks are marked with green circles . (For interpretation of the references to color in this figure legend, the reader is referred to the web version of this article.)

3.1. Framework

Fig. 3 shows the framework of our method. We first compute the gradient images of band images. Then we divide each band image into blocks and select from them using a gradient strength map. We compute similarity measure values between the displaced blocks and the corresponding reference block. In the figure, color maps are used to indicate the NTG values, where the bluest points in the maps correspond to the matching positions. In this way, we obtain the displacements of selected blocks. Finally, we model the

misalignment as a global affine transform and compute the transform parameters.

3.2. Block partition and selection

Our method divides the image into uniformly distributed blocks. In this work the pixel displacement between the reference and floating blocks is limited. This narrows the searching range of optimal discrete pixel displacement in block matching. Compared with the global registration method that searches optimal parameters in the continuous



Fig. 5. Multispectral images (displayed in RGB) used in the synthetic data experiments for registration accuracy evaluation. The images are originally well aligned. Simulated transforms are imposed on all bands except the reference one to generate misaligned multispectral images.

parameter space, our block matching method can be computational efficient.

Fig. 4(d) shows an image divided into $M \times N$ tiled non-overlapping blocks for illustration. For a given image, the number of blocks directly determines the block size. In our method, the block size should be relatively small such that the image registration problem can be simplified to computing the pixel translation from each block pair. On the other hand, the block size should be relatively large such that the corresponding blocks should have sufficient overlapping region. Our investigation indicates that the registration accuracy of our method is insensitive to the number of blocks. Hence we use the setting of $M = N = 8$ in the following presentation. The registration accuracy and computational efficiency of varying numbers of blocks will be shown in the experiments (Section 4.3).

The following block selection and block matching processes both involve gradient images. For a floating image S , we compute its gradients S_x and S_y along the horizontal and vertical directions, respectively, using convolution

$$\begin{aligned} S_x &= \mathbf{h}_x * S, \\ S_y &= \mathbf{h}_y * S, \end{aligned} \quad (1)$$

where the kernels $\mathbf{h}_x = (-0.5, 0, 0.5)$ and $\mathbf{h}_y = (-0.5, 0, 0.5)^T$. Let S_{grad} denote the absolute gradient map of S , the (x, y) th entry in S_{grad} is computed as

$$S_{\text{grad}}(x, y) = |S_x(x, y)| + |S_y(x, y)|. \quad (2)$$

For illustration, a band image and its gradient map are shown in Fig. 4(a) and (b), respectively.

We note that, to keep robustness, only the blocks with sufficient structural information are selected for block matching. It is known that the intensity distributions of two band images can be very different [24]. More specifically, due to the characteristic of scene spectra, the gradient map of one band image may be weak, while that of another band image may be quite strong. This makes the direct use of gradient map inappropriate in block selection. Hence, we compute a gradient strength map F from the gradient map S_{grad} by strengthening the structural information. This is achieved by normalizing S_{grad} and inducing a nonlinear logistic transform.

We compute the mean of gradient map as

$$\mu = \frac{1}{N} \sum_x \sum_y S_{\text{grad}}(x, y), \quad (3)$$

where N denotes the number of pixels. Considering the sparseness of image gradients, μ is quite small in most cases. S_{grad} can be centralized and normalized using μ , producing a normalized gradient map

$$\tilde{S}_{\text{grad}}(x, y) = \frac{S_{\text{grad}}(x, y) - \alpha\mu}{\mu}, \quad (4)$$

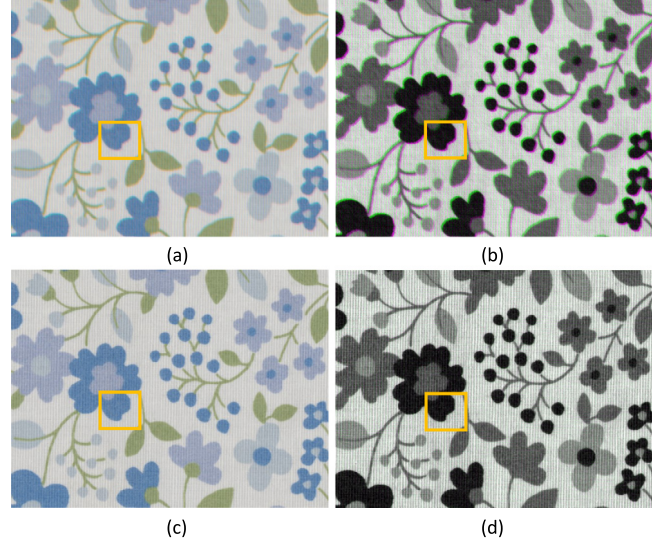


Fig. 6. Registration results of a multispectral image. (a) Original misaligned multispectral image (displayed in RGB), (b) fusion of reference (560 nm) and floating (540 nm) band images from multispectral image in (a), (c) multispectral image after registration, (d) fusion of reference and floating band images from multispectral image in (c). (For interpretation of the references to color in this figure legend, the reader is referred to the web version of this article.)

where parameter $\alpha > 0$ controls the zero position of \tilde{S}_{grad} . By employing the logistical function, the gradient strength map F can be computed as

$$F(x, y) = \frac{1}{1 + \exp(-k\tilde{S}_{\text{grad}}(x, y))}, \quad (5)$$

where parameter $k > 0$ controls the shape of $F(x, y)$. By substituting Eq. (4) into Eq. (5), we have

$$F(x, y) = \frac{1}{1 + \exp\left(-k \frac{S_{\text{grad}}(x, y) - \alpha\mu}{\mu}\right)}. \quad (6)$$

Fig. 4(c) illustrates the curves of function $F(x, y)$ with respect to $S_{\text{grad}}(x, y)$ with different α and k values. With the logistic function, the gradient values around the center $\alpha\mu$, which correspond to the majority of structural information, are approximately scaled. The two ends, which correspond to the quite small and large gradient magnitudes, converge towards the saturation values of 0 and 1, respectively. In this work, we set $\alpha = 2$ and $k = 4$, which produces satisfactory structure extraction results. Fig. 4(d) shows the gradient strength map F . It is observed that the main structures in the band image are well kept while other trivial structures are suppressed.

To improve registration robustness, only blocks with significant structural information are used for local block matching. Let Ω_i denote the pixel domain of the i th block, its significance is computed as

$$I_i = \sum_x \sum_y F(x, y), \quad (7)$$

where $(x, y)^T \in \Omega_i$. We sort all blocks with respect to the values of I_i ($1 \leq i \leq MN$) in descending order, of which the first half are used in the following block matching process. Fig. 4(d) shows the block selection results for illustration.

3.3. Block matching using NTG

We find the displacement of a block pair through block matching. The misalignment between band images is small, and hence the displacement of a block pair lies in a limited range. In this regard, we only estimate the translation, instead of the affine transform between

the block pair. By shifting the floating image block in both horizontal and vertical directions in the range of $[-d, d]$, the similarity measure value is computed between the translated block S' and corresponding reference block T' . Considering the small misalignment between band images, we set $d = 5$, which is sufficient in our system.

Here NTG is employed as the similarity measure because of its effectiveness and efficiency in multispectral image registration [24]. The NTG value between image blocks S' and T' is computed as

$$\text{NTG}(S', T') = \frac{\sum_x \sum_y (|S'_x(x, y) - T'_x(x, y)| + |S'_y(x, y) - T'_y(x, y)|)}{\sum_x \sum_y (|S'_x(x, y)| + |S'_y(x, y)| + |T'_x(x, y)| + |T'_y(x, y)|)}, \quad (8)$$

where S'_x and S'_y denote the gradient images of S' in the horizontal and vertical directions, respectively. T'_x and T'_y are defined similarly. The NTG value reaches minimum when two image blocks are perfectly aligned, while it becomes large when misalignment exists. Hence, the task of estimating the displacement between image blocks is cast as finding the minimum of NTG value.

We compute NTG values at only integer shifting positions. To obtain subpixel accuracy, we interpolate the NTG value grid using bicubic interpolation. By finding the minimum of the grid, we obtain the displacement $(\Delta x, \Delta y)^T$ between the floating and reference image blocks.

3.4. Transform computation

We compute the optimal global affine transform between band images based on the displacements of blocks. We denote the corresponding pixel positions in floating and reference images by $(x, y)^T$ and $(u, v)^T$, respectively. Under the assumption of affine transform, these two positions are related by

$$\begin{pmatrix} u \\ v \end{pmatrix} = \mathbf{P} \begin{pmatrix} x \\ y \\ 1 \end{pmatrix}, \quad (9)$$

where the transform matrix \mathbf{P} is of the form

$$\mathbf{P} = \begin{pmatrix} p_{11} & p_{12} & p_{13} \\ p_{21} & p_{22} & p_{23} \end{pmatrix}. \quad (10)$$

For the i th block in the floating image, the block displacement denoted by $(\Delta x_i, \Delta y_i)^T$ can be obtained following the previous subsection. Let $(x_i, y_i)^T$ denote the center of the block in the floating image, then its corresponding coordinate $(u_i, v_i)^T$ in the reference image can be computed as

$$\begin{aligned} u_i &= x_i + \Delta x_i, \\ v_i &= y_i + \Delta y_i. \end{aligned} \quad (11)$$

We aim to find an optimal transform matrix that minimizes the misalignments of the selected n block pairs. We build a matrix filled with the coordinates x_i and y_i , $1 \leq i \leq n$, as follows

$$\mathbf{X} = \begin{pmatrix} x_1 & y_1 & 1 & 0 & 0 & 0 \\ \vdots & \vdots & \vdots & \vdots & \vdots & \vdots \\ x_n & y_n & 1 & 0 & 0 & 0 \\ 0 & 0 & 0 & x_1 & y_1 & 1 \\ \vdots & \vdots & \vdots & \vdots & \vdots & \vdots \\ 0 & 0 & 0 & x_n & y_n & 1 \end{pmatrix}. \quad (12)$$

We further construct a coordinate vector as

$$\mathbf{u} = (u_1, \dots, u_n, v_1, \dots, v_n)^T. \quad (13)$$

By reordering the elements of \mathbf{P} defined in Eq. (10) into a vector

$$\mathbf{p} = (p_{11}, p_{12}, p_{13}, p_{21}, p_{22}, p_{23})^T, \quad (14)$$

the problem of computing affine transform can be formulated as

$$\mathbf{p}^* = \arg \min_{\mathbf{p}} \{ \|\mathbf{u} - \mathbf{X}\mathbf{p}\|^2 + \lambda \|\mathbf{p}\|^2 \}, \quad (15)$$

where the first term is the sum of fitting errors, and the second term is a regularization preventing too large displacements. The trade-off between these two terms is controlled by the parameter λ . In this work, we set $\lambda = 0.001$. The affine transform can be solved using least squares as

$$\mathbf{p}^* = \mathbf{X}^T \mathbf{u} (\mathbf{X}^T \mathbf{X} + \lambda \mathbf{I})^{-1}. \quad (16)$$

To further improve the robustness of image registration, the RANSAC [30] strategy can be employed to exclude possible outliers. After obtaining \mathbf{p}^* , image registration is accomplished by transforming the pixel coordinates from the floating band image to those of the reference band image.

4. Experimental results

We evaluate the proposed block-based multispectral image registration method on both synthetic and real images. The block-based strategy is compared with the global strategy, on different similarity measures, including mutual information (MI) [31], robust selective normalized cross correlation (RSNCC) [23] and normalized total gradient (NTG) [24]. In addition to quantitative and qualitative evaluation of registration accuracy, an application of spectral color measurement is also given in the experiments.

4.1. Results on synthetic images

The quantitative evaluation of registration accuracy is conducted on synthetic images. Fig. 5 illustrates six well-aligned multispectral images (90 band images to be registered in total) of typical textile fabrics and yarns. Three printing fabric images are shown in the first row, and two yarn-dyed fabric images and one yarn image are shown in the second row. We evaluate the registration accuracy by simulating misaligned multispectral images from these six images. The imposed transforms for simulation are different for individual floating band images. To keep consistency with our real application scenario, in simulated transforms, rotations and scalings are slight while translations are less than 5 pixels.

Fig. 6 shows the registration results of a multispectral image. There are false colors (light blue and purple) around the flowers in the misaligned multispectral image in Fig. 6(a). To visualize the misalignment effect clearly, Fig. 6(b) shows the fusion results of the reference band image (at 560 nm) and a band images (at 540 nm). After registration, chromatic aberration is eliminated, as can be seen in both the multispectral image in Fig. 6(c) and the band fusing result Fig. 6(d).

We define the registration error as the average Euclidean distance between the pixel positions of the reference image and the corresponding positions of the transformed image. Table 1 lists the registration errors of global and block-based registration methods conducted on the multispectral images in Fig. 5. It is observed that, for a given similarity measure, the block-based method usually performs better than its global counterpart. By employing the block strategy and NTG measure, our method yields the lowest registration error (0.175 pixels) averaged on all bands.

In addition to the small misalignment existing in our real application scenario, we also evaluate our method using large displacements. Table 2 lists the registration errors when the simulated translations Δx and Δy are of values $d \in \{4, 8, 12, 16\}$. It is observed that our method achieves high registration accuracy in the case of large displacements.

It is also of our interest to evaluate if our method can deal with slight image magnification in band images. Due to the wavelength-dependent refractive indexes of the lens [11,12], this circumstance may occur if we have not conduct geometric calibration. It actually is not a problem as the affine transform adopted in our method can naturally handle magnification. For illustration, Fig. 7 compares two fusion results before and after image registration when inducing 5% magnification and 3° rotation. This registration capability is sufficient to our real imaging system.

Table 1

Average registration errors (in pixels) of different methods conducted on the multispectral images in Fig. 5. Registration errors at different bands, as well as the averaged band errors, are listed. Note that band No. 9 is the reference band.

	Global MI	Block MI	Global RSNCC	Block RSNCC	Global NTG	Block NTG (Ours)
1	0.647	0.591	0.464	0.123	0.892	0.128
2	0.202	0.151	1.022	0.126	0.749	0.128
3	0.219	0.275	0.883	0.205	0.514	0.195
4	0.194	0.175	0.899	0.127	0.689	0.127
5	0.247	0.175	0.822	0.179	1.300	0.183
6	0.236	0.261	0.848	0.337	0.366	0.313
7	0.191	0.239	0.940	0.237	0.419	0.212
8	0.201	0.140	1.027	0.119	0.179	0.085
9	–	–	–	–	–	–
10	0.223	0.276	1.208	0.314	0.370	0.255
11	0.237	0.255	1.296	0.243	0.293	0.213
12	0.218	0.233	0.763	0.244	0.225	0.206
13	0.220	0.199	0.830	0.199	0.387	0.150
14	0.196	0.184	0.877	0.121	0.286	0.100
15	0.195	0.231	0.747	0.204	0.284	0.159
16	0.291	0.187	0.618	0.159	0.435	0.171
Average	0.248	0.238	0.883	0.196	0.493	0.175

Table 2

Average registration errors (in pixels) produced by our registration method when imposing different transforms on the multispectral images in Fig. 5. The translations in the simulated transforms are all set to the same value d . Registration errors at different bands as well as the averaged band errors are listed. Note that band No. 9 is the reference band.

	$d = 4$	$d = 8$	$d = 12$	$d = 16$
1	0.110	0.116	0.115	0.116
2	0.163	0.159	0.166	0.167
3	0.202	0.189	0.200	0.208
4	0.172	0.177	0.174	0.273
5	0.282	0.272	0.283	0.322
6	0.149	0.151	0.155	0.151
7	0.125	0.117	0.118	0.126
8	0.062	0.056	0.062	0.063
9	–	–	–	–
10	0.141	0.141	0.141	0.137
11	0.216	0.195	0.192	0.188
12	0.123	0.121	0.119	0.127
13	0.195	0.179	0.182	0.188
14	0.134	0.127	0.139	0.143
15	0.133	0.124	0.127	0.131
16	0.176	0.173	0.163	0.177
Average	0.159	0.153	0.156	0.168

Although our method is proposed for aligning multispectral band images, it can also applied to general unimodal images. It is not surprising as the NTG measure, in its nature, can produce high similarity value when two unimodal images are well aligned. Fig. 8 shows such an example.

4.2. Results on real images

We further evaluate our method by acquiring real misaligned multispectral images in the imaging system. Fig. 9 shows the registration results of a printing fabric image. In the original misaligned image, evident orange and blue fringes appear in areas between white and black regions. These fringes disappear after image registration. Fig. 10 illustrates the results of a yarn-dyed fabric image. The fabric is made of red and white yarns. Due to image misalignment, false colors (yellow and purple) are visible in the original image. The sharpness of the boundary between red and white yarns is much improved after image registration. A multispectral image of printed matter is presented in Fig. 11. As a result of chromatic aberrations, perceivable artifacts appear in the image, especially in areas around the eye. After registration, the artifacts are eliminated and good visual appearance is achieved.

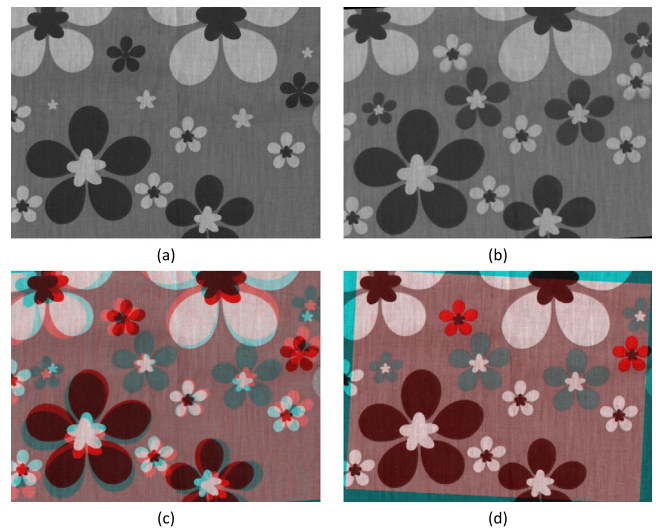


Fig. 7. Registration results of band images with induced magnification and deformation (rotation). (a) Reference band image, (b) floating band image, (c) fusion of reference and floating band images before registration, (d) fusion of reference and floating band images after registration..

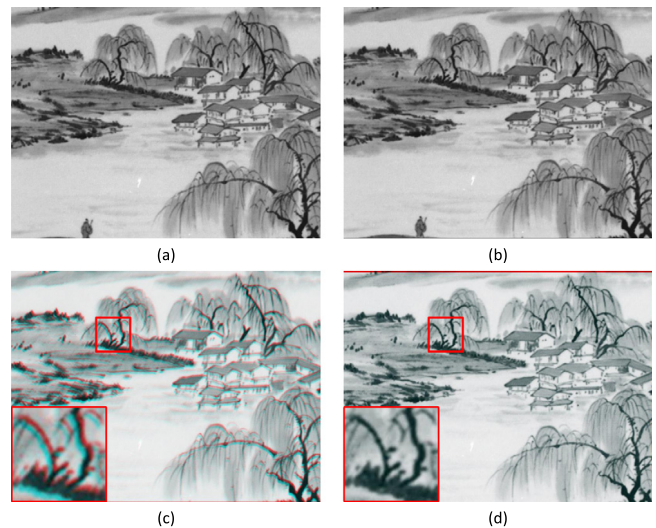


Fig. 8. Registration results of unimodal images. (a) Reference image, (b) floating image, (c) fusion of reference and floating images before registration, (d) fusion of reference and floating images after registration..

4.3. Computational efficiency

The computational efficiency of different methods is evaluated on a multispectral image of 16 bands and 1800×1400 image size. These methods are implemented on a personal computer with Intel(R) Core(TM) i5-2320 CPU at 3.0 GHz and 16 GB RAM using MATLAB R2013a.

We first evaluate our method using varying number ($M \times N$) of blocks, by setting $M = N \in \{6, 8, 12, 16\}$. The average registration errors of varying numbers of blocks are in the range from 0.133 to 0.152 pixels. This indicates that our method is insensitive to the number of blocks. Table 3 lists the execution times when using different number of blocks. It is observed that the execution time increases slightly when $M \times N$ becomes larger.

Then we evaluate the execution times of different methods. The block-based methods adopt the same framework described in Section 3. Table 4 shows that our method costs much less time and the speedups

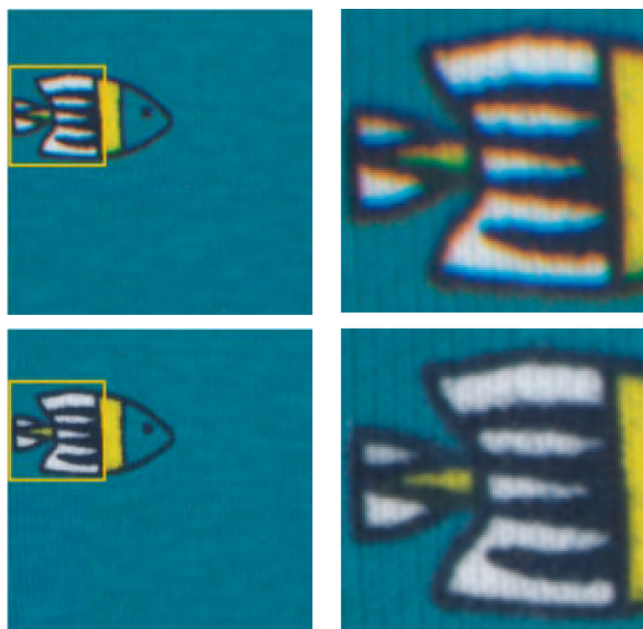


Fig. 9. A multispectral image of a printing fabric before and after registration. First row: original image and its close-up view. Second row: image after alignment and its close-up view. Images are displayed in RGB for visualization. (For interpretation of the references to color in this figure legend, the reader is referred to the web version of this article.)

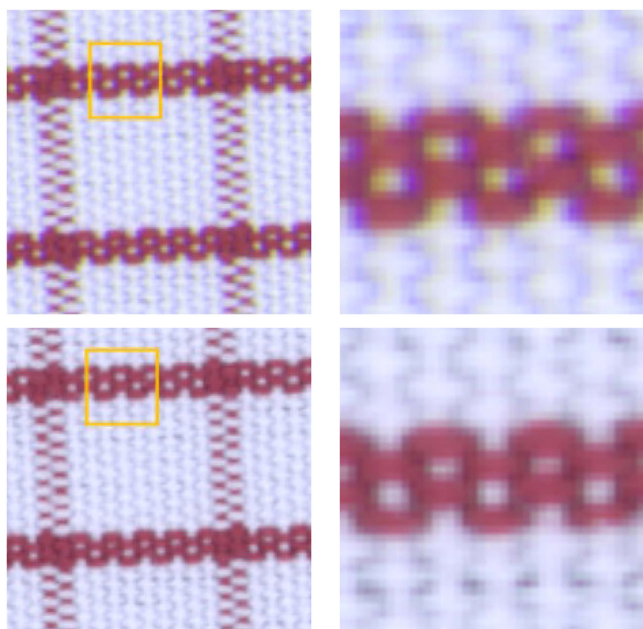


Fig. 10. A multispectral image of a yarn-dyed fabric before and after registration. First row: original image and its close-up view. Second row: image after alignment and its close-up view. Images are displayed in RGB for visualization. (For interpretation of the references to color in this figure legend, the reader is referred to the web version of this article.)

Table 3
Execution times (in seconds) corresponding to varying number of blocks when implementing our method by MATLAB.

	$M = 6$	$M = 8$	$M = 12$	$M = 16$
Time	25.39	26.65	30.57	34.01

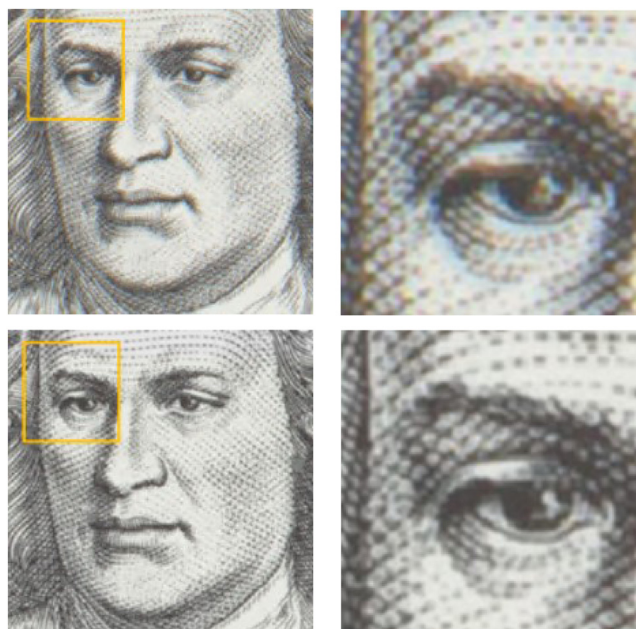


Fig. 11. A multispectral image of a printed matter before and after registration. First row: original image and its close-up view. Second row: image after alignment and its close-up view. Images are displayed in RGB for visualization.

Table 4
Execution times (in seconds) of different methods and the speedups of our method using MATLAB and C++ over other methods. Note that all the methods are implemented using MATLAB unless otherwise noted.

	Time	Speedup (MATLAB)	Speedup (C++)
Global MI	1069.21	40×	319×
Block MI	159.59	6×	47×
Global RSNCC	4032.58	151×	1203×
Block RSNCC	461.53	17×	137×
Global NTG	2365.96	88×	706×
Block NTG (Ours)	26.65 s (MATLAB), 3.35 s (C++)		

over other methods are considerable. When implemented using C++, the execution time is further reduced to 3.35 s, which is sufficient for our practical application.

4.4. Application of spectral color measurement

In our 16-band multispectral imaging system (Fig. 1), the 31-channel spectral reflectance for each pixel is mathematically reconstructed from image intensities using a 31×16 reconstruction matrix. The reconstruction matrix is computed by acquiring 144 color patches and performing Wiener estimation [4]. Spectral color measurement can then be performed based on the reconstructed reflectances of acquired images. Thanks to its fine spatial resolution, our multispectral imaging system can be used for the spectral color measurement of small-sized objects such as textile yarns [32]. However, due to the aforementioned inter-band misalignment, the spectral reflectance is often corrupted, which results in the measurement error. In the following we show that the accuracy of spectral color measurement can be greatly improved with our multispectral image registration method.

Fig. 12 compares the measured spectral reflectances of a white yarn before and after image registration. Red boxes R1 and R3 are in the center area of the yarn, while yellow boxes R2 and R4 are near the edge. The average spectral reflectance of each box is computed from the pixels in that box. Fig. 12(d) shows that, in the original image, the spectral reflectances of boxes R1 and R2 are quite different. The reason is that the reflectance of box R2 is corrupted by image

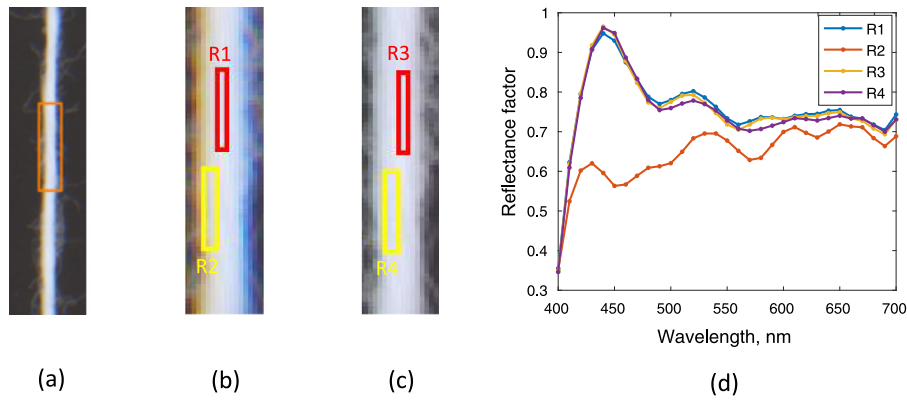


Fig. 12. Spectral color measurement of a white yarn. (a) A single yarn, (b) image before registration, (c) image after registration, (d) spectral reflectance curves of boxes R1–R4 . (For interpretation of the references to color in this figure legend, the reader is referred to the web version of this article.)

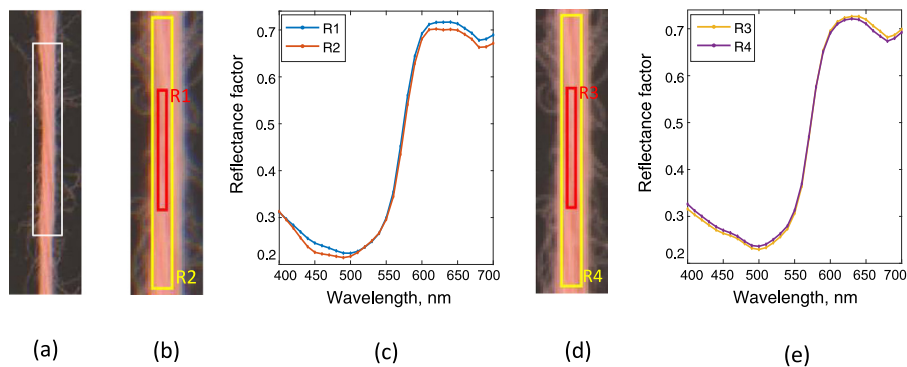


Fig. 13. Spectral color measurement of a pink yarn. (a) A single yarn, (b) image before registration, (c) spectral reflectance curves of boxes R1 and R2. The spectral rms is 0.013 and ΔE_{00} under D65 is 1.211, (d) image after registration, (e) spectral reflectance curves of boxes R3 and R4. The spectral rms is 0.007 and ΔE_{00} under D65 is 0.443 . (For interpretation of the references to color in this figure legend, the reader is referred to the web version of this article.)

Table 5

Spectral root-mean-square (rms) errors and colorimetric errors (ΔE_{00}) under different CIE standard illuminants between the spectral reflectances of R1 and R2 (before registration) as well as those of R3 and R4 (after registration) in Fig. 12.

	Spectral rms	ΔE_{00} (D65)	ΔE_{00} (A)	ΔE_{00} (F2)
Before	0.153	13.770	13.851	14.790
After	0.011	0.504	0.610	0.705

misalignment. After image registration, the spectral reflectance of box R4 becomes very close to that of box R3, indicating the improvement of measurement accuracy.

By setting a spectral reflectance as standard, the difference between two reflectances can be evaluated using both spectral and colorimetric errors. The spectral error is computed as the root-mean-square (rms) between two spectral reflectances. The colorimetric errors are computed using the CIEDE2000 color difference formula [33] under CIE standard illuminants D65, A, and F2, respectively. Table 5 shows the spectral and colorimetric errors of the spectral reflectances in Fig. 12. It is observed that spectral rms error drops from 0.153 to 0.011 after image registration. The color difference error under D65 reduces from 13.770 to 0.504 units.

Fig. 13 shows the spectral color measurement of a pink yarn. Slight chromatic aberration exists in the original image. Red boxes R1 and R3 contain the central part of the yarn, while yellow boxes R2 and R4 contain a larger part. The spectral reflectance curves of R3 and R4 (after registration) in Fig. 13(e) are much closer to each other, compared with those of R1 and R2 (before registration) in (c). Table 6 lists quantitative

Table 6

Spectral root-mean-square (rms) errors and colorimetric errors (ΔE_{00}) under different CIE standard illuminants between the spectral reflectances of R1 and R2 (before registration) as well as those of R3 and R4 (after registration) in Fig. 13.

	Spectral rms	ΔE_{00} (D65)	ΔE_{00} (A)	ΔE_{00} (F2)
Before	0.013	1.211	0.993	1.082
After	0.007	0.443	0.425	0.420

results, indicating the obvious reduction of spectral and colorimetric errors after applying image registration.

5. Conclusion

We have proposed a block-based multispectral image registration method to eliminate the misalignments between band images in a filter-wheel multispectral imaging system. We first divide the band image into blocks and choose part of them using a gradient strength map. Then we compute the displacements of blocks using NTG as the similarity measure. Finally we compute the global affine transform and align the band images. Experimental results illustrate the high accuracy and fast running speed of our method. The method compensates the chromatic aberration in acquired images, and its application to spectral color measurement considerably reduces both spectral and colorimetric errors. The proposed method is quite effective for imaging systems suffering from inter-band misalignments.

Funding

National Natural Science Foundation of China (NSFC) (61371160); Zhejiang Provincial Natural Science Foundation of China (LY18F0-10007).

References

- [1] D. Steen, D. Dupont, Defining a practical method of ascertaining textile color acceptability, *Color Res. Appl.* 27 (6) (2002) 391–398.
- [2] G.A. Shaw, H.K. Burke, Spectral imaging for remote sensing, *Linc. Lab. J.* 14 (1) (2003) 3–28.
- [3] R.M. Levenson, J.R. Mansfield, Multispectral imaging in biology and medicine: slices of life, *Cytometry A* 69 (8) (2006) 748–758.
- [4] H.-L. Shen, P.-Q. Cai, S.-J. Shao, J.H. Xin, Reflectance reconstruction for multispectral imaging by adaptive Wiener estimation, *Opt. Express* 15 (23) (2007) 15545–15554.
- [5] A.A. Mansouri, F.S. Marzani, J.Y. Hardeberg, P. Gouton, Optical calibration of a multispectral imaging system based on interference filters, *Opt. Eng.* 44 (2) (2005) 027004.
- [6] J.Y. Hardeberg, F.J. Schmitt, H. Brettel, Multispectral color image capture using a liquid crystal tunable filter, *Opt. Eng.* 41 (10) (2002) 2532–2549.
- [7] I. Chang, Acousto-optic tunable filters, *Opt. Eng.* 20 (6) (1981) 206824.
- [8] A. Wagadarikar, R. John, R. Willett, D. Brady, Single disperser design for coded aperture snapshot spectral imaging, *Appl. Opt.* 47 (10) (2008) B44–B51.
- [9] N.A. Hagen, M.W. Kudenov, Review of snapshot spectral imaging technologies, *Opt. Eng.* 52 (9) (2013) 090901.
- [10] J. Shen, Y. Chen, Z. Ding, S. Chang, C. Tao, F. Wu, Y. Li, Z. Zheng, Development of energy correction based multishot snapshot spectral imaging system, *Opt. Commun.* 432 (2019) 116–122.
- [11] H.-L. Shen, Z.-H. Zheng, W. Wang, X. Du, S.-J. Shao, J.H. Xin, Autofocus for multispectral camera using focus symmetry, *Appl. Opt.* 51 (14) (2012) 2616–2623.
- [12] S.-J. Chen, H.-L. Shen, Multispectral image out-of-focus deblurring using interchannel correlation, *IEEE Trans. Image Process.* 24 (11) (2015) 4433–4445.
- [13] R.N. Pfisterer, S.D. Vorndran, Color correction strategies in optical design, in: *International Optical Design Conference 2014*, Vol. 9293, International Society for Optics and Photonics, 2014, p. 92931R.
- [14] B.F.C. de Albuquerque, J. Sasian, F.L. de Sousa, A.S. Montes, Method of glass selection for color correction in optical system design, *Opt. Express* 20 (13) (2012) 13592–13611.
- [15] S.Y. Ryu, J.-W. You, Y. Kwak, S. Kim, Design of a prism to compensate the angular-shift error of the acousto-optic tunable filter, *Opt. Express* 16 (22) (2008) 17138–17147.
- [16] H. Zhao, Z. Wang, G. Jia, Y. Zhang, Z. Xu, Chromatic aberrations correction for imaging spectrometer based on acousto-optic tunable filter with two transducers, *Opt. Express* 25 (20) (2017) 23809–23825.
- [17] J. Brauers, N. Schulte, T. Aach, Multispectral filter-wheel cameras: geometric distortion model and compensation algorithms, *IEEE Trans. Image Process.* 17 (12) (2008) 2368–2380.
- [18] Ž. Špiclin, J. Kutrašnik, M. Bürmen, F. Pernuš, B. Likar, Geometric calibration of a hyperspectral imaging system, *Appl. Opt.* 49 (15) (2010) 2813–2818.
- [19] J. Brauers, T. Aach, Geometric calibration of lens and filter distortions for multispectral filter-wheel cameras, *IEEE Trans. Image Process.* 20 (2) (2011) 496–505.
- [20] P. Zhou, H. Zhao, S. Jin, N. Li, Accurate band-to-band registration of AOTF imaging spectrometer using motion detection technology, *Opt. Commun.* 367 (2016) 192–198.
- [21] N.T. Clancy, D. Stoyanov, D.R. James, A. Di Marco, V. Sauvage, J. Clark, G.-Z. Yang, D.S. Elson, Multispectral image alignment using a three channel endoscope in vivo during minimally invasive surgery, *Biomed. Opt. Express* 3 (10) (2012) 2567–2578.
- [22] D.G. Lowe, Distinctive image features from scale-invariant keypoints, *Int. J. Comput. Vis.* 60 (2) (2004) 91–110.
- [23] X. Shen, L. Xu, Q. Zhang, J. Jia, Multi-modal and multi-spectral registration for natural images, in: *European Conference on Computer Vision*, Springer, 2014, pp. 309–324.
- [24] S.-J. Chen, H.-L. Shen, C. Li, J.H. Xin, Normalized total gradient: a new measure for multispectral image registration, *IEEE Trans. Image Process.* 27 (3) (2018) 1297–1310.
- [25] J.J. Moré, The Levenberg-Marquardt algorithm: implementation and theory, in: *Numerical Analysis*, Springer, 1978, pp. 105–116.
- [26] P.J. Van Laarhoven, E.H. Aarts, Simulated annealing, in: *Simulated Annealing: Theory and Applications*, Springer, 1987, pp. 7–15.
- [27] E. Zitzler, L. Thiele, Multiobjective evolutionary algorithms: a comparative case study and the strength Pareto approach, *IEEE Trans. Evol. Comput.* 3 (4) (1999) 257–271.
- [28] C. Fookes, A. Maeder, Optimal grid point selection for improved nonrigid medical image registration, in: *Medical Imaging: Image Processing*, Vol. 5370, International Society for Optics and Photonics, 2004, pp. 1187–1195.
- [29] S.P. Robertson, E. Weiss, G.D. Hugo, A block matching-based registration algorithm for localization of locally advanced lung tumors, *Med. Phys.* 41 (4) (2014) 041704.
- [30] R. Raguram, J.-M. Frahm, M. Pollefeys, A comparative analysis of RANSAC techniques leading to adaptive real-time random sample consensus, in: *European Conference on Computer Vision*, Springer, 2008, pp. 500–513.
- [31] F. Maes, A. Collignon, D. Vandermeulen, G. Marchal, P. Suetens, Multimodality image registration by maximization of mutual information, *IEEE Trans. Med. Imaging* 16 (2) (1997) 187–198.
- [32] L. Luo, H.-L. Shen, S. Shao, J.H. Xin, Empirical model for matching spectrophotometric reflectance of yarn windings and multispectral imaging reflectance of single strands of yarns, *J. Opt. Soc. Amer. A* 32 (8) (2015) 1459–1467.
- [33] M.R. Luo, G. Cui, B. Rigg, The development of the CIE 2000 colour-difference formula: CIEDE2000, *Color Res. Appl.* 26 (5) (2001) 340–350.